

Resonant field amplification with feedback-stabilized regime in current driven resistive wall mode

Yueqiang Liu,^{1,a)} M. S. Chu,² Y. In,³ and M. Okabayashi⁴

¹*Euratom/CCFE Fusion Association, Culham Science Centre, Abingdon OX14 3DB, United Kingdom*

²*General Atomics, San Diego, California 92186-5608, USA*

³*FAR-TECH, Inc., 3550 General Atomics Court, San Diego, California 92121, USA*

⁴*Princeton Plasma Physics Laboratory, Princeton, New Jersey 08543-0451, USA*

(Received 5 May 2010; accepted 27 May 2010; published online 19 July 2010)

The stability and resonant field response of current driven resistive wall modes are numerically studied for DIII-D [J. L. Luxon, *Nucl. Fusion* **42**, 614 (2002)] low pressure plasmas. The resonant field response of the feedback-stabilized resistive wall mode is investigated both analytically and numerically, and compared with the response from intrinsically stable or marginally stable modes. The modeling qualitatively reproduces the experimental results. Furthermore, based on some recent results and on the indirect numerical evidence in this work, it is suggested that the mode stability behavior observed in DIII-D experiments is due to the kink-peeling mode stabilization by the separatrix geometry. The phase inversion radius of the computed plasma displacement does not generally coincide with the radial locations of rational surfaces, also supporting experimental observations. [doi:10.1063/1.3455540]

I. INTRODUCTION

The resistive wall mode (RWM), being a global magnetohydrodynamics (MHD) instability, is one of the key performance limiting factors for many plasma scenarios in fusion devices. Originating from the ideal external kink mode, the RWM can be driven unstable either by the plasma equilibrium pressure (both magnitude and gradient) or by the plasma equilibrium current (largely gradient).

In the reversed field pinch (RFP) devices, the mode is normally current driven and is associated with nonresonant harmonics. This mode, when unstable, is the key factor responsible for an early termination of the discharge in many RFP plasmas. Active control of the RWM has been convincingly demonstrated in several machines,^{1,2} where a large number of magnetic coils are installed outside the thin vacuum vessel. These experiments provide valuable knowledge on how to control this mode using magnetic feedback, not only for the RFPs but also for future tokamak devices such as ITER.³

In present and future advanced tokamak operations, the pressure driven RWM is a significant issue because the mode limits the achievable plasma pressure and thus the fusion power production. Feedback stabilization of the RWM is foreseen as one of the critical routes to achieving high β , steady state plasmas in ITER.⁴ This option has also been extensively pursued in present tokamak experiments, in particular in DIII-D.⁵⁻⁸

The active control experiments in DIII-D high beta plasmas have been very successful. However, the RWM dynamics in these experiments is often complicated, partly due to the plasma rotation and/or the kinetic effects on the mode stability,⁹ and also due to a rather rich interaction between the RWM and other modes.⁸ In order to gain a “clean” un-

derstanding of the RWM behavior under the feedback control in tokamak conditions, specific, current driven RWMs were formed and feedback controlled in DIII-D, at low plasma pressure and slow plasma rotation.¹⁰ Under these conditions, the kinetic effects on the mode are minimized. From the control point of view, there is probably no critical difference between the current and the pressure driven RWMs. [There can be qualitative differences in the internal mode structure (the plasma displacement), as will be shown in this work. The difference in the external mode structure (the perturbed magnetic field), which is what we measure to feed into the control loop, is quantitative and not strongly pronounced.] In fact, most of the analytic models¹¹⁻¹⁴ for the RWM feedback are either based on the current driven case, or does not assume any nature of the mode instability. These models seem to yield qualitatively the same predictions for the mode control behavior as that for the pressure driven case.

We point out, however, that even the current driven RWM control is not truly clean. The DIII-D experiments¹⁰ show a strong interaction between the direct mode control and the error field (EF) correction. Since this interaction also occurs (probably in a more pronounced form) in the pressure driven RWM control, understanding this issue is of crucial importance for designing the feedback systems in future fusion devices. This is one of the issues addressed in this modeling work. In particular, we examine the plasma resonant amplification (RFA) effect in the presence of a feedback-stabilized RWM and compare this response with that of an intrinsically stable mode. The RFA phenomena can have significant impacts on many other plasma related issues, such as the plasma momentum damping and the (dynamic) EF correction.

Compared to the classical current driven kink analysis studied by Shafranov¹⁵ and Wesson,¹⁶ we consider the real-

^{a)}Electronic mail: yueqiang.liu@ccfe.ac.uk.

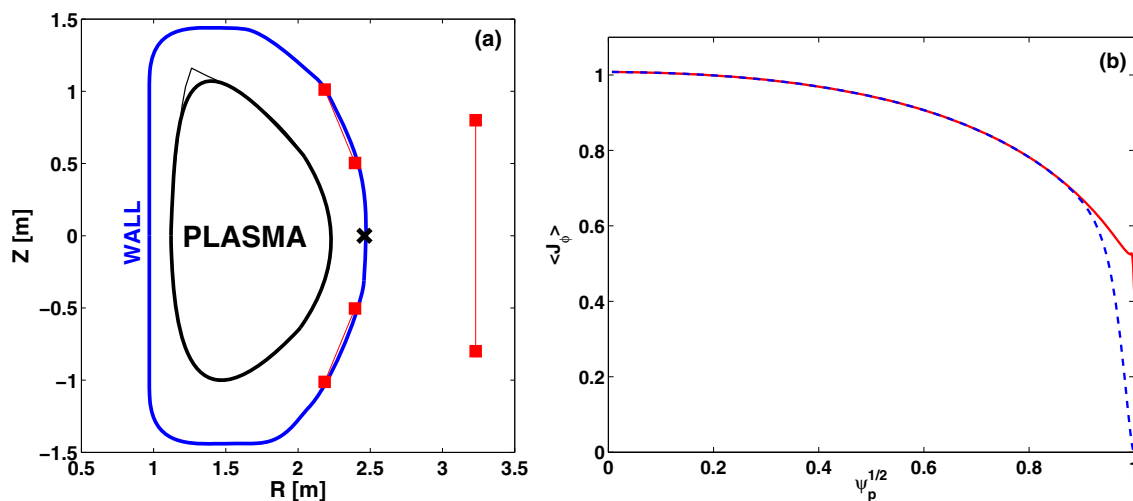


FIG. 1. (Color online) The equilibrium and geometry used in the RWM modeling for DIII-D. (a) The plasma boundary shape with an X-point (thin line) in the experiment and the smoothed boundary (thick line) used in the modeling, the wall shape, the locations of the upper and lower sets of I-coils (just inside the wall) and the C-coils (outside the wall), and the pointwise sensor coil location ("x"). (b) Two profiles of the surface averaged toroidal equilibrium current density used in the modeling. The solid line corresponds to the experimental profile. ψ_p is the normalized poloidal flux.

istic toroidal geometry with strongly shaped plasma (realistic plasma equilibria). The single fluid, ideal MHD code MARS-F (Ref. 17) is used for the modeling. The computed plasma internal structure (displacement) and the current ratio in the feedback and the dynamic EF correction coils allow a direct comparison with experiments.

Section II describes the plasma equilibrium and geometry used in the modeling. Section III reports the kink stability computations and the internal mode structure for these current driven modes in DIII-D. The internal structures are compared with that of a pressure driven kink mode. Section IV is devoted to the study of the RWM response. In particular, the RFA response of feedback-stabilized RWM is analyzed. Section V draws conclusions.

II. EQUILIBRIUM AND GEOMETRY

We consider an equilibrium reconstructed from the DIII-D discharge 133021. Figure 1 shows the plasma boundary shapes and the surface-averaged equilibrium toroidal current profiles. The experimental plasma shape has an upper X-point. Our numerical code, based on a flux coordinate, cannot resolve exactly the X-point, so we instead smooth the plasma boundary near that singularity. This procedure modifies the stability of the kink-peeling mode, as will be discussed later. The experimental plasma current profile has a finite surface current density. We consider both the experimental profile and a profile with a vanishing plasma edge current density [dashed curve in Fig. 1(b)]. The safety factor q has a monotonic radial profile. The equilibrium plasma pressure nearly vanishes, so that the kink instability is driven by the plasma current gradient. In the numerical investigation, we consider a series of equilibria by varying the total plasma current, and hence the edge q value, keeping the current density profile (as well as the plasma boundary shape) fixed.

For the RWM response computations, we use both the internal and the external (with respect to the wall) sets of

coils as shown in Fig. 1(a). These coils have the same geometrical locations in the (R, Z) -plane, as the DIII-D I-coils and C-coils. As for the sensor signal, we assume an internal poloidal field sensor or a pointwise radial field sensor, located at the outboard midplane and at the wall minor radius, as shown in Fig. 1(a).

Figure 2 shows the measured toroidal rotation profile, based on the charge exchange recombination spectroscopy using carbon-VI emission line. This profile is also used in the RWM modeling in this work. The rotation frequency ω_{rot} here is normalized by the Alfvén frequency $\omega_A \equiv B_0 / (R_0 \sqrt{\mu_0 \rho_0})$, with B_0 , R_0 , and ρ_0 being the toroidal magnetic field, the major radius, and the density at the plasma center, respectively. The plasma rotates rather slowly in these experiments.

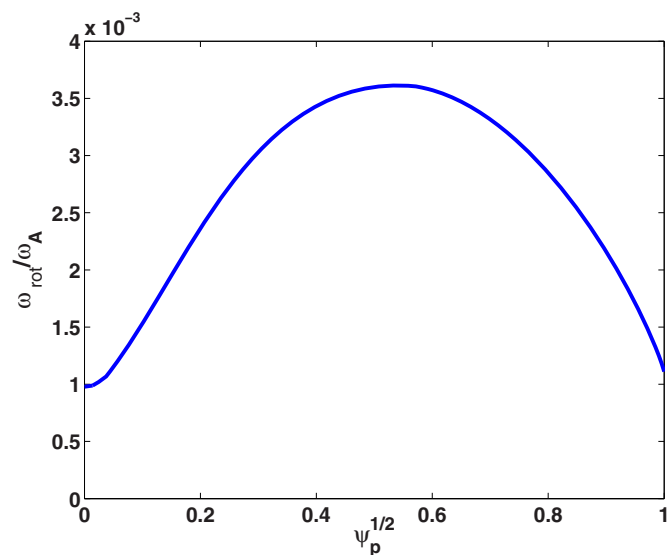


FIG. 2. (Color online) The toroidal rotation profile from DIII-D 133021.

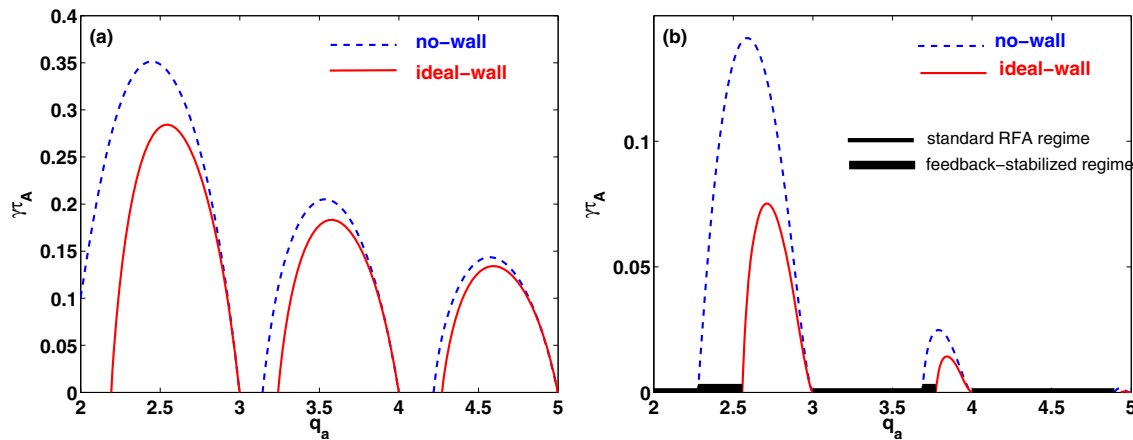


FIG. 3. (Color online) The MARS-F computed growth rate of the ideal kink mode vs the plasma edge safety factor q_a , with (solid) and without (dashed) the ideal wall, for (a) the equilibrium with the experimental current density profile (finite plasma surface current density) and (b) the equilibrium with vanishing current density at the plasma edge. These two current density profiles are shown in Fig. 1(b). Thick solid lines in (b) indicate regions of standard RFA regime for the intrinsically stable mode and regions of feedback-stabilized regime for the RWM, respectively.

III. KINK STABILITY AND MODE STRUCTURE

A. Stability

Using the smoothed plasma boundary shape and the experimental current profile (finite edge current density), we first compute the stability of the ideal external kink mode by scanning over the edge q value q_a (i.e., scaling the total plasma current). The growth rates γ , normalized by the Alfvén time $\tau_A \equiv 1/\omega_A$, are plotted in Fig. 3(a). The stability is compared without a wall and with an ideal conducting wall having the DIII-D wall shape shown in Fig. 1(a). These results resemble that from the classical kink-peeling analysis.

However, the DIII-D experimental data suggest that the mode is stable at $q_{95} > 4$,¹⁸ contradicting the above numerical prediction. (Because of the boundary smoothing used in the modeling, the q_a value from the modeling roughly corresponds to the experimental q_{95} .) One plausible reason is the stabilizing effect of the separatrix on the kink-peeling mode,^{19,20} whose instability is caused by the finite surface current density. Indeed, as shown in Ref. 20, the peeling mode growth rate $\gamma \propto \sqrt{q/q'}$. As q' approaches infinity faster than q toward the separatrix $\gamma \rightarrow 0$, i.e., the peeling mode becomes marginally stable in the presence of an X-point.

In the modeling, one possible approach to eliminate the peeling mode contribution, without inclusion of the separatrix

geometry, is to make the edge current density vanish. This approach is adopted in this work. Certainly this approach does not model the “true” plasma in the experiments. However, we argue that from the viewpoint of the RWM control and response calculations, which is the topic of this study, this procedure is reasonable. One reason is that the peeling component normally has a rather localized mode structure near the plasma edge, as shown in Sec. III B. Moreover, being associated normally with a high poloidal harmonic number, the field perturbation from the peeling component decays very fast outside the plasma surface, leaving an insignificant interaction with the resistive wall. The latter is also evident from Fig. 3(a), showing that the ideal (DIII-D) wall brings little stabilizing effect on the mode for q_a exceeding 4.

By assuming a current profile with vanishing edge density, shown by the dashed line in Fig. 1(b), the instability of the ideal kink mode is significantly reduced for both $q_a > 4$ and $q_a \sim 4$. This is shown in Fig. 3(b). Only a marginally unstable kink mode is obtained at q_a close to 5. These stability results seem to agree better with experimental observations. We emphasize again that in experiments, the mode is stable *not* due to elimination of the drive term (edge current density), but probably thanks to the X-point stabilization.

TABLE I. Three cases for comparison of the mode structure.

	Case no.		
	A	B	C
$\langle J_\phi \rangle_a$	>0	$=0$	>0
q_{\min}	2.38	1.78	2.16
q_a	4.61	3.78	5.95
β_N	0.10	0.14	3.55
$\psi_p^{(q)}$	$\psi_p^{(3,4)} = 0.543, 0.898$	$\psi_p^{(2,3)} = 0.332, 0.913$	$\psi_p^{(3,4,5)} = 0.392, 0.708, 0.895$
Mode	Current driven kink-peeling	Current driven kink	Pressure driven kink
$\gamma\tau_A$	0.143	0.024	0.120

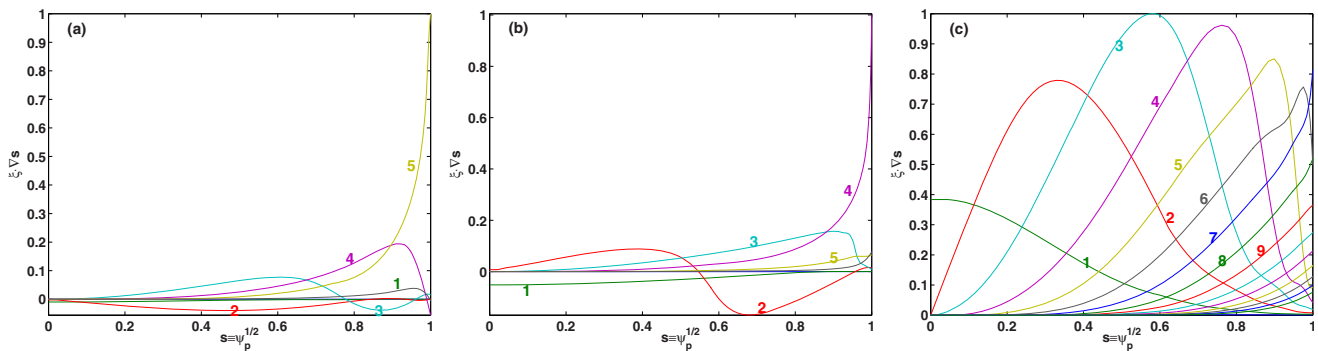


FIG. 4. (Color online) The poloidal Fourier harmonics of the computed plasma displacement $\xi^l \equiv \xi \cdot \nabla s$ for the three equilibria from Table I: (a) case A, (b) case B, and (c) case C. ψ_p is the normalized equilibrium poloidal flux. The numbers in the plots indicate the poloidal harmonic number. Only dominant harmonics are shown. A PEST-like straight-field-line coordinate system is used.

Thick lines in Fig. 3(b) indicate two different RFA regimes—the standard regime where the mode is intrinsically stable, and the feedback-stabilized regime where the RWM is unstable without active control. The plasma response in these two regimes will be compared in Sec. IV. As a final remark, we point out here that for a pressure driven RWM, the unstable RWM can be stabilized either by feedback, or by plasma toroidal rotation and/or drift kinetic effects. In the latter case, we expect the standard RFA response also in the RWM regime.

B. Internal mode structure

We present here a comparison of the internal mode structure (the plasma normal displacement) between the current driven ideal kink-peeling mode and the kink mode, as well as the pressure driven kink mode. Some of the qualitative features can be measured in experiments, e.g., by the electron-cyclotron emission (ECE), and compared with the modeling results.

We choose three cases (equilibria), summarized in Table I. The finite surface current density $\langle J_\phi \rangle|_a > 0$ corresponds to the current profile shown by the solid curve in Fig. 1(b). The vanishing surface current density $\langle J_\phi \rangle|_a = 0$ corresponds to the current profile shown by the dashed curve. The radial location of the rational surfaces (for the toroidal mode $n=1$)

is denoted by $\psi_p^{(q)}$. The equilibrium C is obtained by scaling the plasma pressure amplitude, fixing the pressure and current profiles.

Figures 4(a)–4(c) compare the MARS-F computed eigenmode structure for the three equilibria from Table I. Plotted are the radial profiles of the poloidal Fourier harmonics, for the plasma radial displacement, in the PEST-like straight-field-line flux coordinates, in which Jacobian $J \sim R^2$.²¹ Case A has a dominant peelinglike component, with the poloidal mode number $m=5$. The other harmonics have much lower amplitudes. Case B is a normal, current driven ideal external kink mode. The dominant mode ($m=4$) has smaller mode number. (This is partially caused by the fact that q_a is smaller for this case.) The other harmonics have larger amplitudes toward the plasma core region. Finally, case C results in an unstable pressure driven ideal kink mode. The eigenmode has much richer poloidal spectrum, with all the harmonics having the same sign along the minor radius.

Figures 5(a)–5(c) compare the radial profiles of the plasma displacement, summed over all Fourier harmonics, from the low-field-side (LFS) (at poloidal angle $\chi=0$) and from the high-field-side (HFS) ($\chi=\pi$). A fixed toroidal angle $\phi=0$ is chosen. We notice several qualitative features: (i) there are multiple zero-crossings, corresponding to the phase inversion for the displacement or the perturbed temperature; (ii) for the current driven kink mode (cases A and B), the

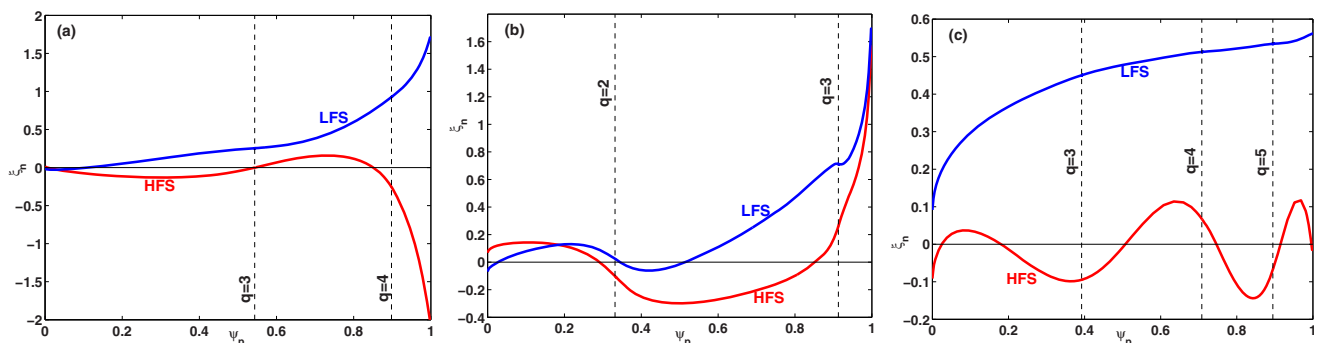


FIG. 5. (Color online) The computed LFS and HFS normal plasma displacement $\xi_n^F \equiv \xi \cdot \nabla s / |s|$ for the three equilibria from Table I: (a) case A, (b) case B, and (c) case C. ψ_p is the normalized equilibrium poloidal flux. The dashed vertical lines indicate the radial location of $q=m(n=1)$ rational surfaces.

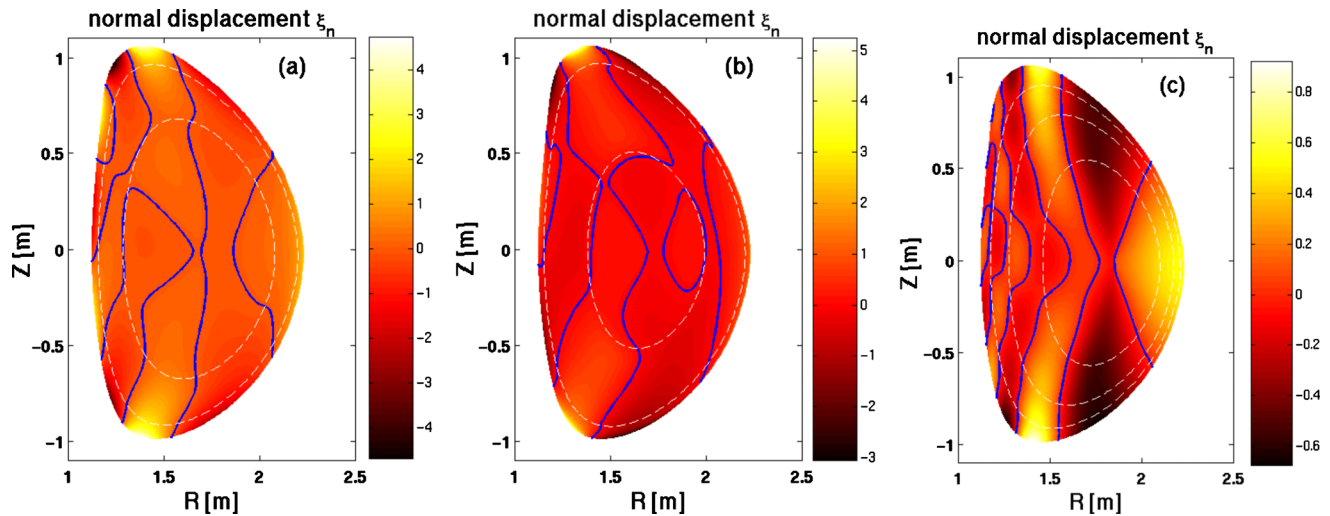


FIG. 6. (Color online) The 2D contour plot, in the R - Z plane, of the computed normal plasma displacement $\xi_n \equiv \xi \cdot \nabla s / |s|$ for the three equilibria from Table I: (a) case A, (b) case B, and (c) case C. The thin dashed lines indicate the rational surfaces. The thick solid lines correspond to contour curves of $\xi_n = 0$.

phase inversion occurs on both the LFS and HFS; for the pressure driven kink mode, the phase inversion occurs only on the HFS; (iii) the radial location, where the phase inversion occurs (i.e., the inversion radius), does not generally coincide with the location of rational surfaces. (The HFS displacement for case A accidentally coincides with the $q=3$ surface location; however, a systematic q_a scan shows that this is not generally the case); and (iv) for current driven kink or kink-peeling mode, the phase inversion normally occurs near one of the rational surfaces.

The above features are also observed in the two-dimensional (2D) contour plots in the R - Z plane, shown in Figs. 6(a)–6(c). These features seem to confirm the experimental ECE measurements for the internal structure.¹⁰ In addition, Figs. 6(a) and 6(b) show that the current driven kink mode causes maximal plasma displacement near the top and bottom regions of the plasma cross section. The pressure driven kink mode [Fig. 6(c)] causes large displacement also near the midplane LFS, reflecting the kink-ballooning nature of the mode. No phase inversion occurs in a large poloidal section at the LFS.

So far we have been showing the mode structure at a specific toroidal angle $\phi=0$. Figure 7 shows the 2D plots in a constant Z plane cutting through the magnetic axis. Again the inversion radius for ideal modes does not generally coincide with the rational surface radius. The distance between these two radii varies with the toroidal angle.

The computed internal mode structure may help interpreting experimental data obtained, e.g., from ECE measurements. (We assume that ECE can measure the temperature perturbation $\delta T = \xi \cdot \nabla T_0$, with the equilibrium temperature T_0 being a monotonic function of the minor radius.) For high pressure plasmas, a phase inversion of the measured temperature perturbation, *in the LFS*, should indicate a resistive mode, whereas the absence of the phase inversion should suggest an ideal mode. However, it is questionable to reach the same mode identification, if the ECE measurement is taken *from the HFS*. Moreover, the inversion radius may not actually indicate the location of the rational surface.

For low pressure plasmas, the situation can be more complicated at both HFS and LFS. It is possible that a phase inversion occurs for either ideal or resistive modes. Since for

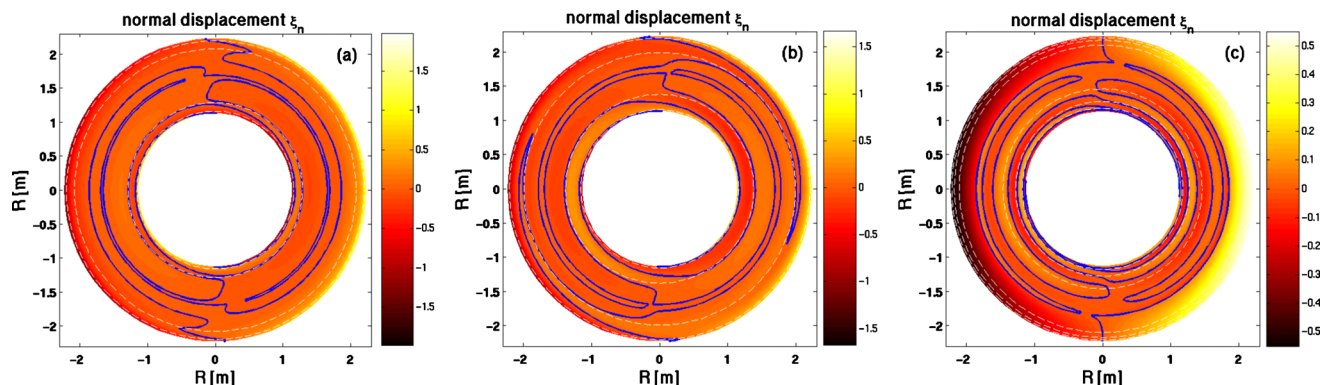


FIG. 7. (Color online) The 2D contour plot, in the $Z=\text{const}=Z_{\text{axis}}$ plane, of the computed normal plasma displacement $\xi_n \equiv \xi \cdot \nabla s / |s|$ for the three equilibria from Table I: (a) case A, (b) case B, and (c) case C. The thin dashed lines indicate the rational surfaces. The thick solid lines correspond to contour curves of $\xi_n = 0$.

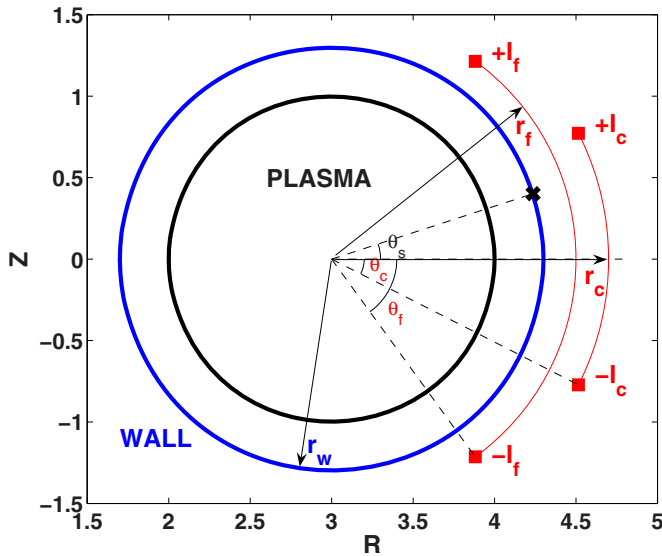


FIG. 8. (Color online) A sketch of the coils geometry in a cylindrical model for the RFA response of feedback-stabilized RWM. Both feedback coils (with current I_f) and the RFA coils (with current I_c) are present.

the ideal mode, the inversion radius generally does not coincide with the location of the rational surface, an independent measurement, such as the q profile, helps to identify whether the mode is a resistive mode. In case the ideal mode (e.g., the RWM) has different frequency than the resistive mode, the frequency measurement provides additional mode identification.

Finally, we mention that the zero-crossing of the normal displacement for ideal modes has been studied in the literature. For instance, for a cylindrical plasma, Newcomb's theorem states that the configuration is stable if and only if the normal displacement has no zero in each subinterval between two adjacent rational surfaces,²² meaning that an unstable mode allows zero-crossing outside rational surfaces. It has been noticed in Ref. 23 that an $m=1$ internal kink mode can have multiple zero-crossings (nodes) depending on the mode growth rate. These nodes are near the rational surface location but do not necessarily coincide with it.

IV. RESPONSE OF FEEDBACK-STABILIZED RWM

Figure 3(b) shows that by decreasing the q_a value (e.g., during a current ramp-up), the plasma first experiences a stable response to EFs or external fields produced by coil currents. As q_a is below 4, there can be a response of marginally stable RWM. Further decrease of q_a (below 3) causes a strongly unstable kink mode (or RWM for $2.277 < q_a < 2.556$). The DIII-D experiments show that these modes can be feedback-stabilized using the I-coils. A particular interest is to understand the RFA response of the feedback-stabilized RWM. We first present an analytic model for a cylindrical circular plasma, followed by detailed numerical results for the DIII-D equilibria.

A. A cylindrical model

Consider a cylindrical plasma with the circular cross section. Figure 8 shows the coil configuration. The feedback

coil, with the coil current I_f , spans a poloidal angle of $2\theta_f$. The RFA coil, with the coil current I_c , spans a poloidal angle of $2\theta_c$. A pointwise sensor is located at a poloidal angle $\theta = \theta_s$. The minor radii of the plasma boundary, the wall, the feedback, and the RFA coils are denoted by a , r_w , r_f , and r_c , respectively. We assume that the sensor is located on the wall.

We derive rigorously the RFA response transfer function of the feedback-stabilized RWM on this cylindrical example. The case, with $a < r_w < r_f < r_c$ and with the pointwise radial sensor, is considered. The other cases (various radial locations of the feedback and RFA coils with respect to the wall, radial versus internal/external poloidal sensors) can be derived in a similar fashion.

The following list of conditions is our starting point for the derivation.^{13,14}

- (i) The ideal force balance condition at the plasma-vacuum interface

$$\left. \frac{rb'_{rm}}{b_{rm}} \right|_{a+} = C_m, \quad (1)$$

where C_m is a constant to be determined.

- (ii) The field jump condition across the thin wall

$$\left. \frac{r[b'_{rm}]}{b_{rm}} \right|_{r_w} = 2s\tau_w, \quad (2)$$

where s is the Laplace variable and τ_w is the penetration time of the $m=1$ field through the wall.

- (iii) In the absence of the feedback and RFA coils ($I_f=I_c=0$), we have $s=\Gamma_m$, the growth/damping rate of the RWM. This growth/damping rate can be computed analytically for certain cylindrical equilibria.¹³ We assume here that Γ_m is a known quantity.
- (iv) For the case of the feedback-stabilized RWM, when an external current I_c , at a real frequency ω_c , is applied to the plasma, the mode evolution should follow the excitation frequency. Thus, at steady state, we have $s=i\omega_c$.
- (v) Finally, a feedback logic needs to be specified. We assume a current control scheme, with the following feedback law:

$$b_0^f = -Kb_r^s, \quad (3)$$

where the feedback gain K is chosen to stabilize the mode. b_0^f is the free-space field produced by the feedback coil current I_f , as shown in Fig. 8, at the location ($r=r_w$, $\theta=0$). We use this quantity for the normalization purposes, as well as for denoting the feedback current in the control law. The poloidal component of this free-space field is calculated via a geometrical factor f_m^f (Ref. 13),

$$b_{rm}^f = f_m^f b_0^f, \quad (4)$$

$$f_m^f \equiv \frac{m}{2|m|} \frac{\sin(m\theta_f) r_w^2 + r_f^2 - 2r_w r_f \cos \theta_f}{\sin \theta_f r_f^2}.$$

In Eq. (3), b_r^s denotes the radial sensor signal, which is the sum of all the poloidal Fourier harmonics at the poloidal location of the sensor

$$b_r^s = \sum_m b_{rm}^s \exp(im\theta_s). \quad (5)$$

Our goal is to calculate the response model P of the feedback-stabilized RWM, defined as

$$P(i\omega_c) \equiv \frac{b_r^s(i\omega_c)}{b_0^c}, \quad (6)$$

where b_0^c is the free-space field produced by the RFA coil current I_c at the location ($r=r_w$, $\theta=0$). The poloidal component of this field is calculated in a similar way as for b_0^f ,

$$b_{rm}^c = f_m^c b_0^c, \quad f_m^c \equiv \frac{m \sin(m\theta_c) r_w^2 + r_c^2 - 2r_w r_c \cos \theta_c}{2|m| \sin \theta_c r_c^2}. \quad (7)$$

We first consider the general case with $I_f \neq 0$ and $I_c \neq 0$. The total radial field in the vacuum region between the plasma and the wall is

$$b_{rm}(r) = b_{rm}^p \left(\frac{r}{a}\right)^{-\mu-1} + b_{rm}^w \left(\frac{r}{r_w}\right)^{\mu-1} + b_{rm}^f \left(\frac{r}{r_f}\right)^{\mu-1} + b_{rm}^c \left(\frac{r}{r_c}\right)^{\mu-1}, \quad (8)$$

where $\mu \equiv |m|$. Condition (i) gives

$$\frac{\mu-1-C_m}{\mu+1+C_m} \left(\frac{a}{r_w}\right)^{\mu-1} = \frac{b_{rm}^p}{b_m}, \quad (9)$$

$$b_m \equiv b_{rm}^w + b_{rm}^f \left(\frac{r_w}{r_f}\right)^{\mu-1} + b_{rm}^c \left(\frac{r_w}{r_c}\right)^{\mu-1}. \quad (10)$$

Condition (ii) leads to

$$-2\mu b_{rm}^w = 2s\tau_w b_{rm}^s = 2s\tau_w \left[b_m + b_{rm}^p \left(\frac{a}{r_w}\right)^{\mu+1} \right]. \quad (11)$$

In the special case with $I_f=I_c=0$, $b_m=b_{rm}^w$, and $s=\Gamma_m$, Eqs. (9) and (11) are combined to yield

$$\frac{\mu-1-C_m}{\mu+1+C_m} \left(\frac{a}{r_w}\right)^{2\mu} = -\frac{\Gamma_m \tau_w + \mu}{\Gamma_m \tau_w}. \quad (12)$$

In the general case with $I_f \neq 0$, $I_c \neq 0$, and $s=i\omega_c$, Eqs. (9) and (12) give

$$\frac{b_{rm}^p}{b_m} = -\frac{\Gamma_m \tau_w + \mu}{\Gamma_m \tau_w} \left(\frac{a}{r_w}\right)^{-\mu-1}. \quad (13)$$

Hence

$$b_{rm}^s = b_m + b_{rm}^p \left(\frac{a}{r_w}\right)^{\mu+1} = -\frac{\mu}{\Gamma_m \tau_w} b_m = -\frac{\mu}{i\omega_c \tau_w} b_{rm}^w, \quad (14)$$

where Eq. (11) has been taken into account. The last equality in Eq. (14), together with the definition of b_m in Eq. (10), results in

$$b_{rm}^w = \frac{-i\omega_c}{i\omega_c - \Gamma_m} \left[b_{rm}^f \left(\frac{r_w}{r_f}\right)^{\mu-1} + b_{rm}^c \left(\frac{r_w}{r_c}\right)^{\mu-1} \right]. \quad (15)$$

This leads to an update of the feedback law (3),

$$b_0^f = -K \sum_m \frac{\mu}{i\omega_c \tau_w - \Gamma_m \tau_w} \left[\left(\frac{r_w}{r_f}\right)^{\mu-1} f_m^f b_0^f + \left(\frac{r_w}{r_c}\right)^{\mu-1} f_m^c b_0^c \right] \exp(im\theta_s), \quad (16)$$

$$= -K [P_f(i\omega_c) b_0^f + P_c(i\omega_c) b_0^c], \quad (17)$$

where

$$P_g(s) \equiv \sum_m \frac{\mu(r_w/r_g)^{\mu-1}}{s\tau_w - \Gamma_m \tau_w} f_m^g, \quad g=f,c \quad (18)$$

is precisely the transfer function of the plasma response model as defined in Refs. 13 and 14, for external active coils with radial sensors.

Equation (17) facilitates the last step to obtain the plasma RFA response of the feedback-stabilized RWM,

$$P(i\omega_c) \equiv \frac{b_r^s}{b_0^c} = \frac{1-b_0^f}{b_0^c K} = \frac{P_c(i\omega_c)}{1+KP_f(i\omega_c)}. \quad (19)$$

Knowing the transfer functions $P_f(s)$ and $P_c(s)$, the plasma RFA response $P(i\omega_c)$ is easily computed using Eq. (19), provided that the controller gain K is chosen such that the closed loop system is stable. The same Eq. (19) can be derived for various geometrical configurations of the feedback/RFA coils and the sensor types.

Equation (19) allows a transparent physics interpretation for the case of a single mode plasma response. Assuming there is only one mode in the plasma, with the open-loop growth rate Γ_0 , the transfer functions $P_f(s)$ and $P_c(s)$ can then be written as

$$P_f(s) = \frac{R_f}{s\tau_w - \Gamma_0 \tau_w}, \quad P_c(s) = \frac{R_c}{s\tau_w - \Gamma_0 \tau_w}, \quad (20)$$

where the residues R_f and R_c characterize the (geometrical) coupling between the mode and the feedback and RFA coils, respectively. The RFA response of the feedback-stabilized mode, according to Eq. (19), becomes

$$P(i\omega_c) = \frac{R_c}{i\omega_c \tau_w - \Gamma_0 \tau_w + KR_f} = \frac{R_c}{i\omega_c \tau_w - \Gamma_f \tau_w}, \quad (21)$$

where $\Gamma_f \equiv \Gamma_0 - KR_f/\tau_w$ is the damping rate of a new mode that responds to the RFA coils. On the other hand, by solving the characteristic equation $1+KP_f(s)=0$ for the closed loop system, we find that the damping rate of the feedback-stabilized RWM, at large enough feedback gain, does coincide with Γ_f . This agrees with our physics understanding of the RFA response for a generic stable mode.

B. Toroidal results

Equation (19), though derived in a cylindrical geometry, also holds for toroidal plasmas. This can be understood by realizing that the total sensor signal b^s , in the presence of

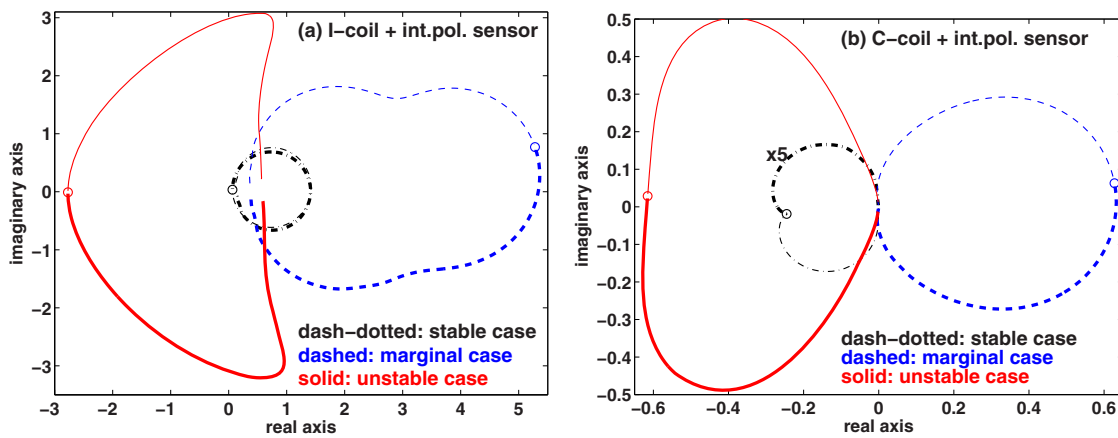


FIG. 9. (Color online) Nyquist plots of the plasma response transfer functions for stable (dashed-dotted, $q_a=4.5$), marginally stable (dashed, $q_a=3.664$), and unstable (solid, $q_a=2.416$) RWM. The equilibria correspond to Fig. 3(b). The internal poloidal sensor, located just inside the DIII-D vacuum vessel [see Fig. 1(a)], is considered in combination with (a) the I-coils and (b) the C-coils. The toroidal phase difference between the upper and the lower sets of I-coils is assumed to be 240° . The stable (dashed-dotted) response shown in (b) is amplified by a factor of 5.

both feedback and RFA coils, is the sum of the plasma response b_f^s caused by the feedback current, and the plasma response b_c^s caused by the RFA coil current. Hence

$$b_0^f = -Kb^s = -K(b_f^s + b_c^s) = -K(b_0^f P_f + b_0^c P_c), \quad (22)$$

resulting in Eq. (19).

Furthermore, denoting the free-space mutual inductance between the feedback (RFA) coil and the sensor coil by M_{fs} (M_{cs}), we have

$$b_0^f = M_{fs} I_f, \quad b_0^c = M_{cs} I_c. \quad (23)$$

Substituting Eq. (23) into Eq. (22), we obtain the current ratio between the feedback current and the RFA coil current

$$\frac{I_f}{I_c} = -\frac{M_{cs}}{M_{fs}} \frac{K P_c}{1 + K P_f}, \quad (24)$$

valid for general toroidal cases.

Equation (19) shows that in a general toroidal geometry, by computing the transfer functions $P_f(s)$ and $P_c(s)$ for the feedback coils and RFA coils separately, we can construct the plasma response from a feedback-stabilized RWM. In the following, these transfer functions are computed using the MARS-F code for both the DIII-D I-coils and C-coils. We choose three equilibria from Fig. 3(b), with $q_a=4.5$, 3.664, and 2.416, corresponding to a stable, marginally stable, and unstable RWM, respectively. The choice of $q_a=2.416$ leads to a RWM mode that is halfway between the no-wall and the ideal-wall limits in terms of q_a [see Fig. 3(b)]. The choice of these three cases is motivated by DIII-D experiments,¹⁸ where different stability/instability domains are accessed with the q_a variation. We mention that in experiments, a robust feedback stabilization of the mode at q_{95} below 3 is still challenging.

Figures 9(a) and 9(b) plot the MARS-F computed transfer function $P_g(i\omega_c)$ in the complex plane, as the excitation frequency ω_c varies from $-\infty$ to $+\infty$. [The transfer function from toroidal computations is defined in the similar way to the cylindrical theory (6).] The thin lines indicate negative $\omega_c < 0$ and the thick lines indicate positive ω_c . The open

circles (\circ) indicate $\omega_c=0$. The symbol g denotes either the I-coils (a) or C-coils (b). Internal poloidal sensors are assumed. For an unstable mode, the Nyquist diagram of the open-loop transfer function determines whether the closed feedback loop can be stable with a proportional controller. Both unstable cases shown in Figs. 9(a) and 9(b) can be stabilized by a sufficiently large proportional gain. The maximal amplitude of $P_g(i\omega_c)$ shows how strong the plasma (the RWM) responds to the coils. Clearly the I-coil currents excite a much larger response than the C-coils. The deeply stable RWM (dashed-dotted lines) causes little plasma response with either I-coils or C-coils.

Similar computations have been performed assuming pointwise radial sensors. The corresponding Nyquist diagrams are shown in Fig. 10. The unstable mode can still be stabilized, with a proper choice of proportional gains, with the I-coils. The same mode cannot be feedback-stabilized with the C-coils. Again the (unstable or stable) plasma response to the I-coils is generally stronger than that to the C-coils. For the deeply stable mode (the dashed-dotted lines), the response is close to a unit circle, reflecting the fact that most of the (radial) sensor signal comes from the free-space field of the coils.

We mention that the results shown in Figs. 9 and 10 are not sensitive to the equilibria that we choose. Qualitatively, the same results are obtained by considering three cases (stable, unstable, and marginally stable) from Fig. 3(a).

The difference in the response for stable, marginal, and unstable cases, shown in Figs. 9 and 10, is primarily associated with the mode eigenvalue. In addition, due to the difference in the equilibria (e.g., the q_a value) for these three cases, we expect certain difference in the mode structure, which should also play a role in the plasma response. Figure 11 compares the normal field component for three cases, subject to a unit dc current excitation in I-coils or C-coils. In order to clearly show the response of the mode, we subtracted the free-space field, produced by the same unit current in the coils, from the total response. [We mention that Figs. 9 and 10 show the total plasma response (at the sensor

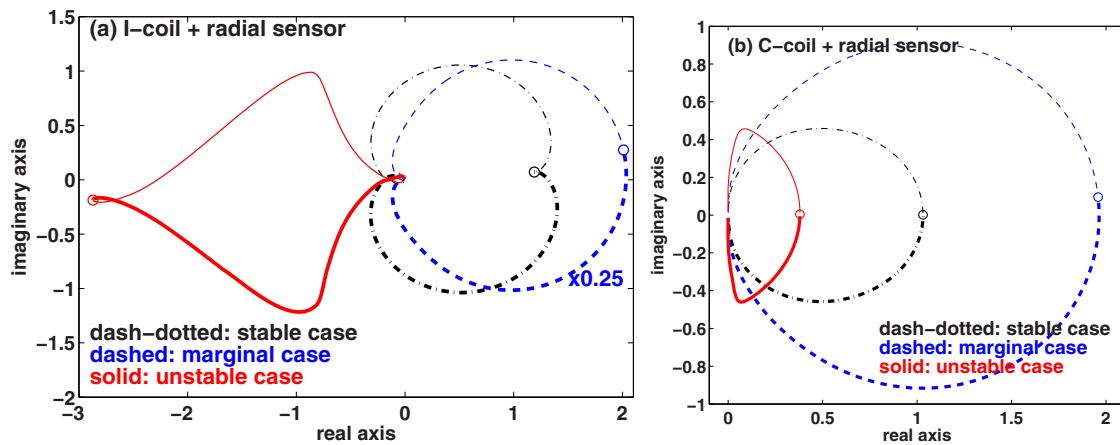


FIG. 10. (Color online) Nyquist plots of the plasma response transfer functions for stable (dash-dotted, $q_a=4.5$), marginally stable (dashed, $q_a=3.664$), and unstable (solid, $q_a=2.416$) RWM. The equilibria correspond to Fig. 3(b). The pointwise radial sensor, located at the outboard midplane [see Fig. 1(a)], is considered in combination with (a) the I-coils and (b) the C-coils. The toroidal phase difference between the upper and the lower sets of I-coils is assumed to be 240° . The marginally stable (dashed) response shown in (a) is reduced by a factor of 4.

location) *without* the subtraction of the vacuum field.] Besides the difference in the mode amplitude (the deeply stable case has one order of magnitude weaker response, the unstable case responds with an opposite sign), we notice indeed certain difference in the mode structure. In particular, the marginally stable mode has a larger response at the HFS (poloidal angle close to $\pm 180^\circ$). The mode structure near the outboard midplane (poloidal angle of about 0°) is similar for all three cases. Comparing Figs. 11(a) and 11(b), we notice that the amplitude of the mode response to the I-coils is roughly 4.5 times larger than that to the C-coils, for all three cases. However, the excited mode poloidal structure is almost identical for I-coils and C-coils.

With a dc current excitation as in Fig. 11, no eddy current is induced in the wall, hence the wall does not affect the mode response. With an ac excitation, however, the wall eddy current also affects the mode response. This is demonstrated in Fig. 12, where a traveling wave, with a frequency $\omega_c \tau_w = 2$ normalized by the longest decay time τ_w of the $n=1$ wall eddy current, is launched in either I-coils or

C-coils. Assuming a wall time of 5 ms for DIII-D, this corresponds to an excitation frequency of about 64 Hz. Figure 12 again compares the mode response, which is the total response subtracted by the *wall* response, for the stable, marginal, and unstable cases. We observe again certain differences and similarities in the mode structure. Compared to the dc case, the amplitude of the mode response is generally twice smaller, with the same unit amplitude of the coil currents. The phase response of the mode to the ac excitation is also affected by the choice of the equilibrium. Comparing Figs. 12(a) and 12(b), we notice some difference in the mode structure excited by the I-coils and C-coils. This difference is larger than the case of the dc excitation and is due to the wall eddy current induced plasma response (the wall eddy current patterns for the I-coils are different from that for C-coils).

A special case that has been extensively investigated in experiments is the plasma response to the dc coil current $\omega_c=0$. Figures 13(a) and 13(b) show the real part of $P_g(\omega_c=0)$ with I-coils and C-coils, respectively. (At slow plasma rotation, $\text{Im}[P_g(\omega_c=0)]$ is normally small as

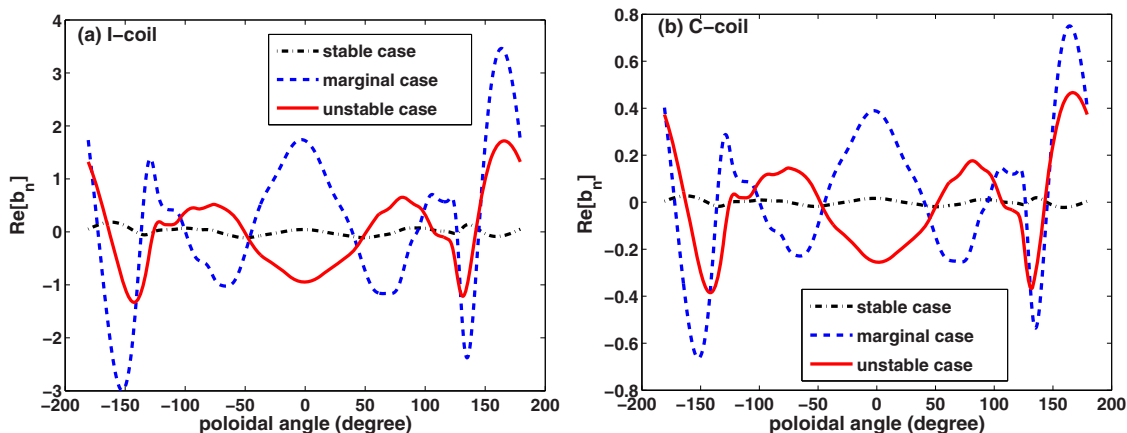


FIG. 11. (Color online) The real part of the normal field component of the excited mode for the stable (dash-dotted, $q_a=4.5$), marginally stable (dashed, $q_a=3.664$), and unstable (solid, $q_a=2.416$) cases. The equilibria correspond to Fig. 3(b). The mode structure is plotted along the wall surface vs the geometrical angle, defined with the magnetic axis as the origin. Compared are the mode response to a unit dc current in (a) I-coils and (b) C-coils. The toroidal phase difference between the upper and the lower sets of I-coils is assumed to be 240° .

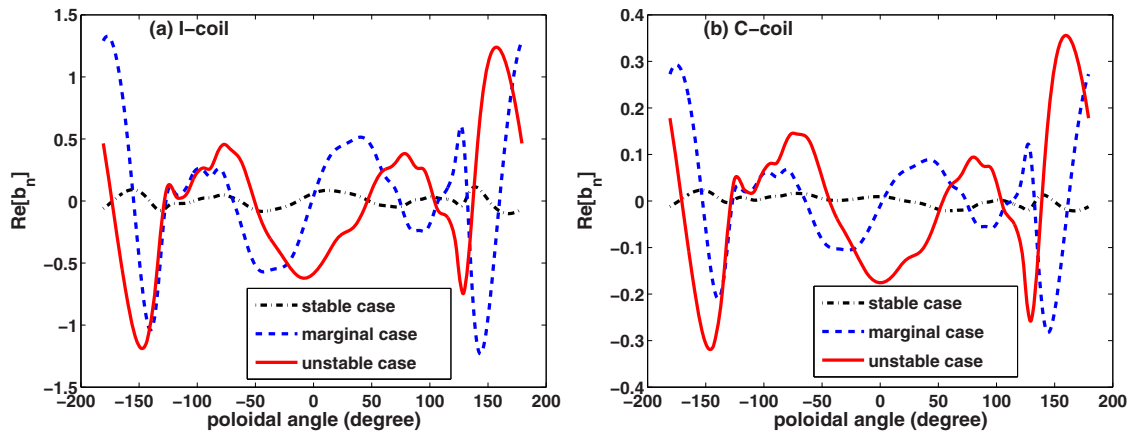


FIG. 12. (Color online) The real part of the normal field component of the excited mode for the stable (dashed-dotted, $q_a=4.5$), marginally stable (dashed, $q_a=3.664$), and unstable (solid, $q_a=2.416$) cases. The equilibria correspond to Fig. 3(b). The mode structure is plotted along the wall surface vs the geometrical angle, defined with the magnetic axis as the origin. Compared are the mode response to a unit ac current in (a) I-coils and (b) C-coils. The excitation frequency is $\omega_c\tau_w=2$. The toroidal phase difference between the upper and the lower sets of I-coils is assumed to be 240° .

shown by Figs. 9 and 10.) A full scan of the equilibria from Fig. 3(b) is made. The q_a scan covers three special regions, $q_a \in [2.277, 2.556]$, $q_a \in [3.687, 3.772]$, and $q_a \in [4.895, 4.937]$, where the mode is unstable without a wall and stable with an ideal wall (i.e., the RWM regime). We observe a sharp variation of $\text{Re}[P_g(\omega_c=0)]$ (switching sign) near the no-wall limits $q_a=2.277$, 3.687 , and 4.985 , indicating a change of the mode stability. A sharp variation, to a lesser degree, is also seen as q_a crosses integer numbers. This is also associated with the change of stability [Fig. 3(b)]. However, it seems the plasma rotation, though slow, efficiently smooths the transition across these marginal points. For the RFA modeling of the RWM response, we do not focus on the transition across integer q_a .

Another interesting observation is that, with C-coils and radial sensors [Fig. 13(b)], the quantity $\text{Re}[P_g(\omega_c=0)]$ quickly switches sign as q_a varies from the no-wall to the ideal-wall limit. This is normally an indication that the unstable RWM is no longer stabilizable with a simple proportional controller. The behavior is qualitatively different with

the I-coils or with the internal poloidal sensors. This shows a limited capability of feedback-stabilizing the RWM, using the C-coils in combination with radial sensors.

Finally, we notice that the plasma response is not sensitive to the change of q_a in regions where the ideal kink mode is intrinsically stable, i.e., where q_a exceeds the integer number but is well below the no-wall limit. Knowing the plasma response transfer functions $P_{f,c}(i\omega_c)$, as shown in Figs. 9 and 10, we can study the current ratio between the direct feedback (DF) current I^{DF} and the current I^{EF} in the EF correction coils (the RFA coils), following Eq. (24). The current ratio can be easily measured in the feedback-RFA experiments. We emphasize that only a simple situation is considered here, where we assume that the EFs are generated by one of the DIII-D coils (I-coils or C-coils), while in experiments, the intrinsic EFs (plus the plasma response to them) are often caused by factors such as the misalignments of the poloidal and toroidal field coils. A more elaborate model can be considered, where a direct control loop for the RWM stabilization (fast feedback), a dynamic control loop for the EF cor-

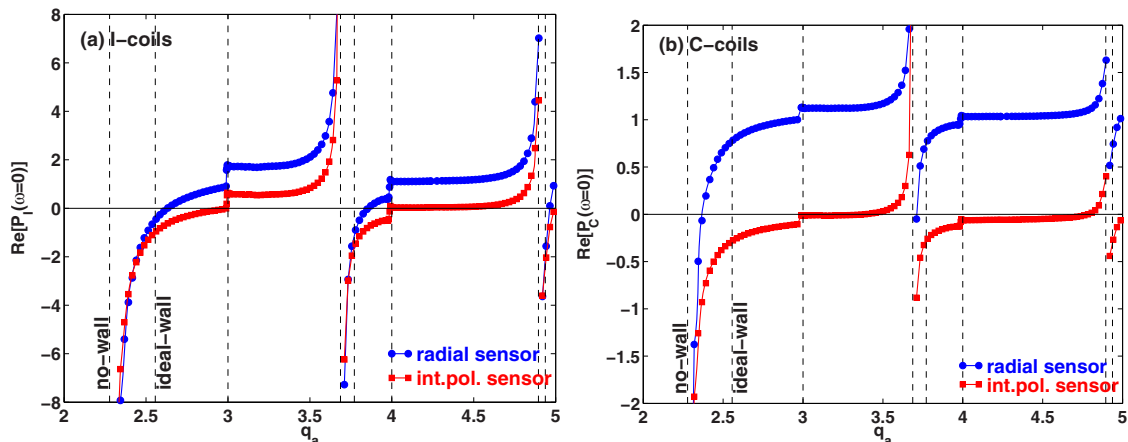


FIG. 13. (Color online) The q_a scan of the plasma response to dc coil currents using (a) I-coils and (b) C-coils. The toroidal phase difference between the upper and the lower sets of I-coils is assumed to be 240° . The response is normalized by the corresponding free-space radial field from the coil currents. The responses detected by internal poloidal sensors and by pointwise radial sensors are compared. Vertical dashed lines indicate the no-wall and ideal-wall marginal stability points, as well as q_a crossing integer numbers.

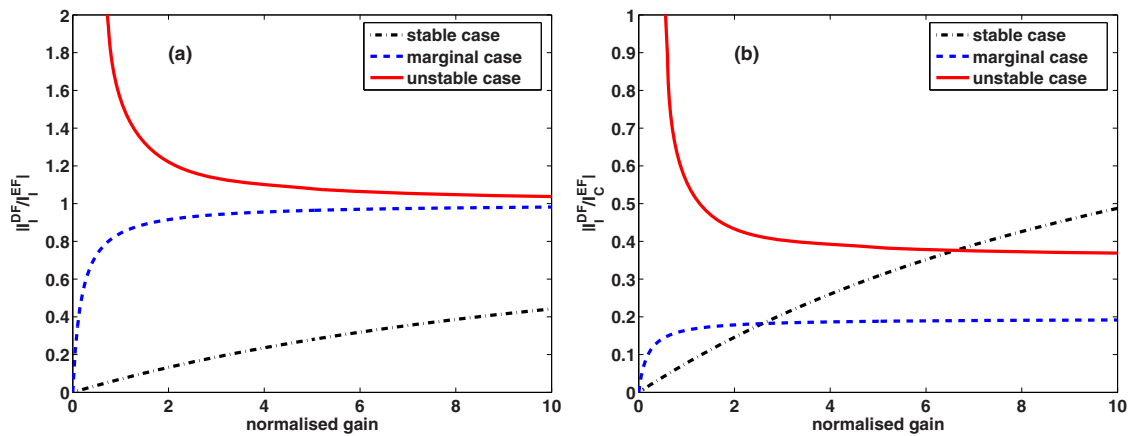


FIG. 14. (Color online) The amplitude ratio of the current response in I-coils (a) to that in I-coils and (b) to that in C-coils. The ratio is plotted against the proportional control gain under the dc condition. The toroidal phase difference between the upper and the lower sets of I-coils is assumed to be 240° . The converged values of the current ratio for case (b), at infinite feedback gain, are shown in (a). Internal poloidal sensors are used in the modeling.

rection (slow feedback), and the intrinsic EFs are all combined. The final results (the current ratio) can still be obtained knowing the transfer functions $P_{f,c}$ and some characteristics of the intrinsic EFs, but will depend on the details of assumptions made into the model, such as the feedback equation(s) such as Eq. (22).

In principle, one can assume that both the I-coils and the C-coils can act either as the DF coils or the EF coils, yielding several possible combinations. We consider two combinations which are likely the closest to experiments. Figure 14(a) shows the results when the I-coils are used both for the DF and for generating the EFs. In this case, $P_f = P_c$. Under the dc condition $\omega_c = 0$, the current ratio (24) becomes a simple function of the feedback gain K . Note that for the intrinsically (open loop) unstable RWM, it makes physics sense to compute the current ratio, only when the feedback gain exceeds the critical value, resulting in a feedback-stabilized RWM. At infinite gain value, all the three curves converge to 1. The convergence rate is considerably faster for the marginally stable case. The deeply stable case converges very slowly to 1.

The second interesting case is to use the I-coils for direct RWM feedback and the C-coils for EF generation. The current amplitude ratio versus the feedback gain, under the dc excitation, is shown in Fig. 14(b). We observe qualitatively similar behavior as in Fig. 14(a), except that the curves do not converge to 1 anymore at infinite gain. This is because these modes, being associated with different q_a values, are different modes, and they respond differently to the coil currents. This means essentially that the residues of the transfer functions $P_{f,c}$ from Eq. (24) vary with q_a .

Figure 15 shows the converged current ratio at infinite gain, as a function of the excitation frequency ω_c , for the second case. The frequency is normalized by the computed longest decay time τ_w of the $n=1$ wall eddy current. Plotted are both the amplitude ratio and the phase difference between the currents in the I-coils and C-coils. For both intrinsically stable and marginally stable modes, the amplitude ratio monotonically decreases with increasing the excitation frequency. For the feedback-stabilized mode, the frequency

behavior is more complicated. The deeply stable case has a large phase shift between the DF I-coil current and the EF C-coil current. However, we should notice that the deeply stable mode causes very little plasma response, as shown by Figs. 9, making the current phase slightly sensitive to the plasma condition.

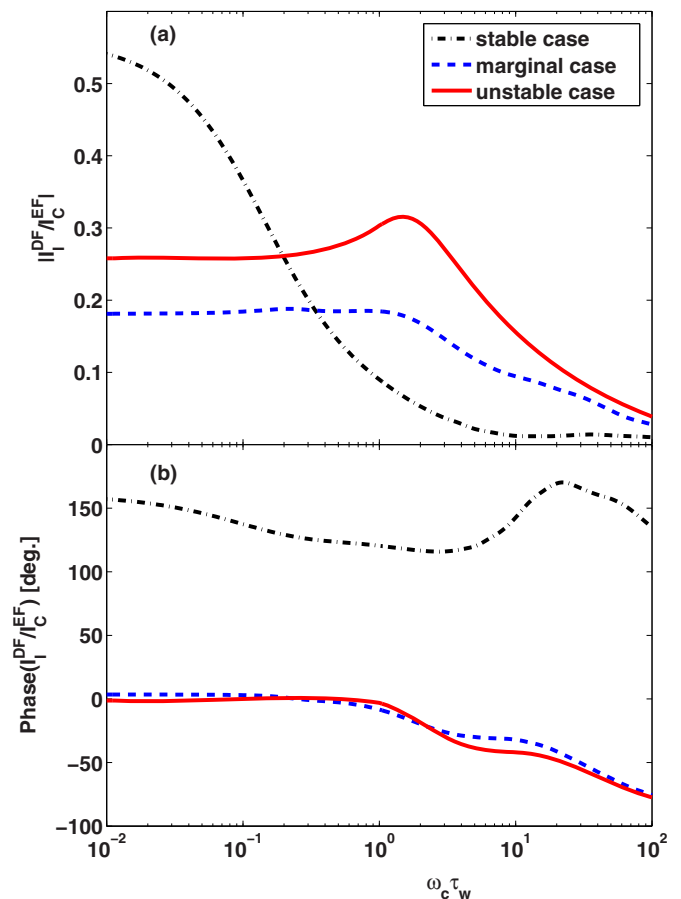


FIG. 15. (Color online) The (a) amplitude ratio and (b) phase difference of the current responses between I-coils and C-coils. The ratio is plotted against the coil current excitation frequency at infinite gain. The toroidal phase difference between the upper and the lower sets of I-coils is assumed to be 240° . Internal poloidal sensors are used in the modeling.

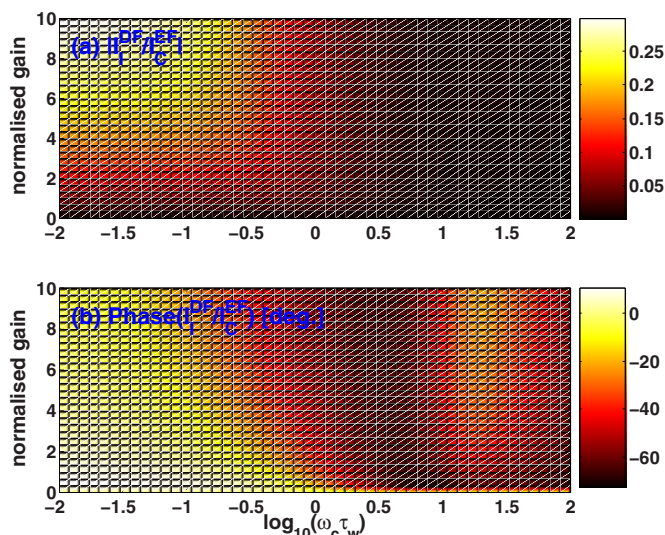


FIG. 16. (Color online) The (a) amplitude ratio and (b) phase difference of the current responses between I-coils and C-coils, for the stable case A. Both the coil current excitation frequency and the proportional control gain are varied. The toroidal phase difference between the upper and the lower sets of I-coils is assumed to be 240° . Internal poloidal sensors are used in the modeling.

Figure 16 shows 2D contour plots of the current amplitude ratio and the phase difference for the deeply stable case, which exhibits the slowest transient behavior. A larger current ratio is achieved at large gain value and with the dc excitation.

V. SUMMARY AND DISCUSSIONS

The current driven RWM in DIII-D plasmas is modeled using the MARS-F code. Since the plasma equilibrium pressure in these plasmas nearly vanishes, it is expected that the drift kinetic effects or the sound wave damping effects on the mode should be negligible, unlike for the pressure driven RWM. The slow plasma rotation also limits the Alfvén continuum damping effect. Therefore, it is expected that these current driven modes can be reasonably well described and studied by ideal MHD theory, as long as the realistic plasma geometry and equilibrium profiles are taken into account.

As a main result, the RFA response of feedback-stabilized RWM, which has been under extensive experimental investigation, is modeled and analytically studied in this work. The computed coil current response, for feedback-stabilized RWM, marginally stable mode, as well as intrinsically stable mode, qualitatively agrees with the experimental observations. This allows a better understanding of the experimental observations. The computed plasma response transfer functions, for I-coils and C-coils, can also be used for the control optimization, for both the DF and the dynamic EF correction. A quantitative comparison between the modeling and the experiments requires a detailed modeling of the feedback scheme used in experiments and a good knowledge (and model) of the EF sources. This will be reported in a future work.

Analytic theory²⁰ suggests that in the presence of a separatrix in the experimental plasma, the peeling mode contri-

bution to the instability, caused by the finite edge current density, diminishes. This seems to explain the experimentally observed stability domain in terms of the edge q value. In the numerical modeling (with a smoothed plasma boundary near the X-point), we remove the peeling mode contribution by eliminating the edge current density.

The computed eigenmode structures are compared for the current driven ideal kink-peeling mode, the kink mode, as well as the pressure driven kink mode. In particular, we find that the phase inversion radius of the plasma displacement, though in many cases close to the locations of the rational surfaces, does not generally coincide with them. Similar observations have been made in DIII-D experiments.¹⁰

ACKNOWLEDGMENTS

Y.Q.L. thanks Dr. T. C. Hender and Dr. R. J. Hastie for valuable discussions on the ideal mode eigenstructure. Dr. T. C. Hender's efforts of careful reading through the manuscript are also gratefully acknowledged.

This work was partly funded by the United Kingdom Engineering and Physical Sciences Research Council under Grant No. EP/G003955 and the European Communities under the contract of association between EURATOM and CCFE. The views and opinions expressed herein do not necessarily reflect those of the European Commission. This work was also supported by the U.S. Department of Energy under Grant No. DE-FG03-956ER54309.

¹P. R. Brunzell, D. Yadikin, D. Gregoratto, R. Paccagnella, T. Bolzonella, M. Cavinato, M. Cecconello, J. R. Drake, A. Luchetta, G. Manduchi, G. Marchiori, P. Marrelli, P. Martin, A. Masiello, F. Milani, S. Ortolani, G. Spizzo, and P. Zanca, *Phys. Rev. Lett.* **93**, 225001 (2004).

²R. Paccagnella, S. Ortolani, P. Zanca, A. Alfieri, T. Bolzonella, L. Marrelli, M. E. Puiatti, G. Serianni, D. Terranova, M. Valisa, M. Agostini, L. Apolloni, F. Auriemma, F. Bonomo, A. Canton, L. Carraro, R. Cavazzana, M. Cavinato, P. Franz, E. Gazza, L. Grando, P. Innocente, R. Lorenzini, A. Luchetta, G. Manduchi, G. Marchiori, S. Martini, R. Pasqualotto, P. Piovesan, N. Pomaro, P. Scarin, G. Spizzo, M. Spolaore, C. Taliercio, N. Vianello, B. Zaniol, L. Zanotto, and M. Zuin, *Phys. Rev. Lett.* **97**, 075001 (2006).

³R. Aymar, P. Barabaschi, and Y. Shimomura, *Plasma Phys. Controlled Fusion* **44**, 519 (2002).

⁴T. C. Hender, J. C. Wesley, J. Bialek, A. Bondeson, A. H. Boozer, R. J. Buttery, A. Garofalo, T. P. Goodman, R. S. Granetz, Y. Gribov, O. Gruber, M. Gryaznevich, G. Giruzzi, S. Guenter, N. Hayashi, P. Helander, C. C. Hegna, D. F. Howell, D. A. Humphreys, G. T. A. Huysmans, A. W. Hyatt, A. Isayama, S. C. Jardin, Y. Kawano, A. Kellman, C. Kessel, H. R. Koslowski, R. J. La Haye, E. Lazzaro, Y. Q. Liu, V. Lukash, J. Manickam, S. Medvedev, V. Mertens, S. V. Mirnov, Y. Nakamura, G. Navratil, M. Okabayashi, T. Ozeki, R. Paccagnella, G. Pautasso, F. Porcelli, V. D. Pustovitov, V. Riccardo, M. Sato, O. Sauter, M. J. Schaffer, M. Shimada, P. Sonato, E. J. Strait, M. Sugihara, M. Takechi, A. D. Turnbull, E. Westerhof, D. G. Whyte, R. Yoshino, H. Zohm, and ITPA MHD, Disruption and Magnetic Control Topical Group, *Nucl. Fusion* **47**, S128 (2007).

⁵A. M. Garofalo, M. S. Chu, E. D. Fredrickson, M. Gryaznevich, T. H. Jensen, L. C. Johnson, R. J. La Haye, G. A. Navratil, M. Okabayashi, J. T. Scoville, E. J. Strait, A. D. Turnbull, and DIII-D Team, *Nucl. Fusion* **41**, 1171(2001).

⁶M. Okabayashi, J. Bialek, M. S. Chance, M. S. Chu, E. D. Fredrickson, A. M. Garofalo, M. Gryaznevich, R. E. Hatcher, T. H. Jensen, L. C. Johnson, R. J. La Haye, E. A. Lazarus, M. A. Makowski, J. Manickam, G. A. Navratil, J. T. Scoville, E. J. Strait, A. D. Turnbull, and M. L. Walker, *Phys. Plasmas* **8**, 2071 (2001).

⁷E. J. Strait, J. M. Bialek, I. N. Bogatu, M. S. Chance, M. S. Chu, D. H. Edgell, A. M. Garofalo, G. L. Jackson, R. J. Jayakumar, T. H. Jensen, O.

- Katsuro-Hopkins, J. S. Kim, R. J. La Haye, L. L. Lao, M. A. Makowski, G. A. Navratil, M. Okabayashi, H. Reimerdes, J. T. Scoville, A. D. Turnbull, and DIII-D Team, *Phys. Plasmas* **11**, 2505(2004).
- ⁸M. Okabayashi, I. N. Bogatu, M. S. Chance, M. S. Chu, A. M. Garofalo, Y. In, G. L. Jackson, R. J. La Haye, M. J. Lanctot, J. Manickam, L. Marrelli, P. Martin, G. A. Navratil, H. Reimerdes, E. J. Strait, H. Takahashi, A. S. Welander, T. Bolzonella, R. V. Budny, J. S. Kim, R. Hatcher, Y. Q. Liu, and T. C. Luce, *Nucl. Fusion* **49**, 125003 (2009).
- ⁹H. Reimerdes, A. M. Garofalo, G. L. Jackson, M. Okabayashi, E. J. Strait, M. S. Chu, Y. In, R. J. La Haye, M. J. Lanctot, Y. Q. Liu, G. A. Navratil, W. M. Solomon, H. Takahashi, and R. J. Groebner, *Phys. Rev. Lett.* **98**, 055001 (2007).
- ¹⁰Y. In, M. Chu, G. L. Jackson, J. S. Kim, R. J. La Haye, Y. Q. Liu, L. Marrelli, M. Okabayashi, H. Reimerdes, and E. J. Strait, "Requirements for active resistive wall mode (RWM) feedback control," *Plasma Phys. Controlled Fusion* (submitted).
- ¹¹M. Okabayashi, N. Pomphrey, and R. E. Hatcher, *Nucl. Fusion* **38**, 1607 (1998).
- ¹²V. D. Pustovitov, *Plasma Phys. Rep.* **27**, 195 (2001).
- ¹³A. Bondeson, Y. Q. Liu, D. Gregoratto, Y. Gribov, and V. D. Pustovitov, *Nucl. Fusion* **42**, 768 (2002).
- ¹⁴Y. Q. Liu, *Plasma Phys. Controlled Fusion* **48**, 969 (2006).
- ¹⁵V. D. Shafranov, *Soviet J. Tech. Phys.* (in Russian) **40**, 241 (1970).
- ¹⁶J. A. Wesson, *Nucl. Fusion* **18**, 87 (1978).
- ¹⁷Y. Q. Liu, A. Bondeson, C. M. Fransson, B. Lennartson, and C. Breitholtz, *Phys. Plasmas* **7**, 3681 (2000).
- ¹⁸M. Okabayashi, Y. In, G. L. Jackson, M. S. Chu, J. Hanson, R. J. La Haye, M. J. Lanctot, Y. Q. Liu, L. Marrelli, P. Martin, J. K. Park, P. Piovesan, L. Piron, H. Reimerdes, A. Soppelsa, E. J. Strait, and RWM Group, "Error field correction in stable/unstable RWM regime—a view of dynamic error field correction," Proceedings of the 15th Meeting of the ITPA MHD Stability Topical Group, 8–12 March 2010, National Institute for Fusion Science, Toki, Japan.
- ¹⁹S. Yu. Medvedev, A. A. Martynov, Y. R. Martin, O. Sauter, and L. Villard, *Plasma Phys. Controlled Fusion* **48**, 927 (2006).
- ²⁰A. J. Webster and C. G. Gimblett, *Phys. Rev. Lett.* **102**, 035003 (2009).
- ²¹R. C. Grimm, J. M. Greene, and J. L. Johnson, *Methods Comput. Phys.* **16**, 253 (1976).
- ²²W. A. Newcomb, *Ann. Phys.* **10**, 232 (1960).
- ²³J. P. Goedbloed and P. H. Sakanaka, *Phys. Fluids* **17**, 908 (1974).